Surface plasmon resonance of a bimetallic nanostructured film for enhanced optical sensitivity

By: Taylor Mabe, Zheng Zeng, Bhawna Bagra, James Ryan, and Jianjun Wei

This is the peer reviewed version of the following article:

T. Mabe, Z. Zeng, B. Bagra, J. Ryan, J. Wei Surface plasmon resonance of a bimetallic nanostructured film for enhanced optical sensitivity, *ChemistrySelect*, **2018**, 3, 3018-3023, DOI: 10.1002/slct.201800576.

which has been published in final form at https://doi.org/10.1002/slct.201800576. This article may be used for non-commercial purposes in accordance with Wiley Terms and Conditions for Use of Self-Archived Versions.

Abstract:

A bimetallic (Ag/Au) nanoslit film is reported on surface plasmon (SP) generation and refractive index (RI) sensitivity. These were compared to gold devices in transmission surface plasmon resonance (tSPR). The bimetallic films have a primary resonant peak that shifts with periodicity and correlates well with Finite-Difference Time-Domain (FDTD) simulation studies. The SPR of bimetallic nanoslit structures is analyzed via a semi-analytical model. The model enables decomposition and quantitative analysis of SP generation at the aperture under plane-wave illumination. The nanostructured, metallic, thin films provide flexibility to integrate with microfluidics, allowing for simplified instrumentation and alignment. Calculation and experimentation demonstrate that bimetallic films afford an increase in RI sensitivity due to the addition of silver along with the biocompatibility of gold. The Ag/Au films were found to be non-diffusing, long-term stable (over several months), and provided an increase in sensitivity (about 53/RIU) over gold equivalents.

Keywords: Bimetallic film | nanoslit structure | optical sensing | refractive index | surface plasmon resonance

Article:

1 Introduction

Greatly enhanced transmission of light through a subwavelength aperture in a patterned metallic film with a regularly repeating periodic structure underlines the physics of the extraordinary transmission (EOT) phenomena,[1] which results in a variety of applications, such as bio-detection and biosensing schemes.[2] Nanostructures and nanostructured metal thin films can utilize the phenomena of surface plasmon resonance (SPR) to detect binding events of biomolecules by

monitoring a refractive index (RI) change. SPR comes in two forms, a localized mode and a propagating mode. Localized surface plasmon resonance (LSPR) is where electrons oscillate back and forth inside of a nanoscale structure,[3] such as nanoparticles,[4] nanotriangles,[5] nanostars,[6] nanohole arrays,[7] nanotriangle arrays,[7] and other shapes.[4,8] The other form is surface plasmon polariton (SPP), which occurs at the interface of a metal and a dielectric. Some techniques are used to accomplish SPP generation with light (photons), including end-fire coupling,[9] high RI prisms,[10] gratings,[10] or nanostructures.[11] A nanostructured planar film has an additional benefit of allowing for transmission mode SPR, which can be easily integrated into microfluidics.[12] Nanostructures in gold planar films have been investigated previously,[13] such as nanohole, nanocircle, and nanoslit arrays. In regards to sensitivity to RI changes near the surfaces, it was found that the nanoslit array was the most sensitive; 16% higher than the nanohole arrays and 5% higher than the nanocircle arrays.[13]

Metals are the materials of choice in plasmonics, since surface plasmons can couple light strongly to the metal surface and thereby greatly enhance light-matter interactions.[14] Other materials being investigated for their plasmonic potential include the alkali metals,[15] transparent conducting oxides,[15] and graphene.[15, 16] A desirable plasmonic material has a large plasma frequency, high conductivity, high polarizability (large $-\epsilon'$), low ohmic loss (small ϵ''), and the ability to fabricate nanostructures in the material.[14] Only a few materials are effective at generating surface plasmons.[17] Copper has interband transitions below 600 nm and oxidizes. Aluminum is good in the UV region but also forms oxides. Silver has the highest conductivity, longest SPP propagation distances, and the highest quality factor in the visible region. Gold has interband transitions below 480 nm[18] and is the workhorse of SPR due to its chemical inertness. Compared to gold, silver has higher electromagnetic (EM) fields in the sensing area and less attenuation of its SPP generation. Silver has an added benefit of being shifted to longer wavelengths, into the window of 0.6 μm-1.2 μm. This region is outside of the biological auto-fluorescence region and therefore has an advantage of free of biological interference. A single metal does not possess all of the traits of a high quality plasmonic material, but a bimetallic chip potentially could. A device composed of silver and gold could incorporate the optical and electrical properties of silver underneath an inert layer of gold.

The bimetallic nanostructures provide composition-tunable plasmonic resonances for plasmon-based sensing and surface field-enhanced spectroscopy,[19] and various structures such as core-shell nanoparticles,[20] nanoholes,[21] and nanorods.[22] Du et al. performed a theoretical investigation of a planar bimetallic SPR chip and found a 20% increase in the evanescent field strength and an 80% increase in the sensitivity compared to the gold control chip.[19a] Sharma et. al. presented a theoretical study of bimetallic nanoparticles and found that the sensitivity was tunable with metal ratio and that Ag/Au had the highest sensitivity of the alloys.[19c] The Sohn group found that a bimetallic device was twice as accurate as gold equivalents, with peak widths half that of the gold.[19d] They also showed a two-fold increase in sensitivity and a six-fold improvement in limit of detection (LOD).[19e] Ong et al. discerned that a bimetallic film had a two-fold improvement in sensitivity over gold.[19f] Multilayers of gold–silver array on prisms show SPR enhanced near-field fluorescence from quantum dots deposited at the surface of these platforms.[19h] Murray-Me'thot et al. experimentally demonstrated the improved optical properties of Au/Ag bimetallic nanohole arrays over pure Au or Ag nanohole arrays and found the dependence of excitation wavelength, the RI sensitivity, and the transmission full width at half-maximum (FWHM) on the

metal compositions.[21] Kim et al. reported the tunability of surface plasmon by composition variation in nanorod structures and investigated the metallic composite impact on both the far-field and near-field scattering spectra.[22]

The efficiency of surface plasmon (SP) generation of bimetallic systems and its effect on the sensitivity are rarely explored. This study presents an investigation of bimetallic (Ag/Au) nanoslit films with a focus on optical properties and RI sensitivity as a comparison to pure gold nanoslit films in light transmission measurements. A semi-analytical analysis and a Finite-Difference Time-Domain (FDTD) simulation were used to estimate the SP generation and optical response, respectively, for providing a fundamental understanding of the dielectric sensitivity of these devices. The findings in this work show that bimetallic nanostructures can be attuned to enhance the sensitivity in surface plasmon resonance.

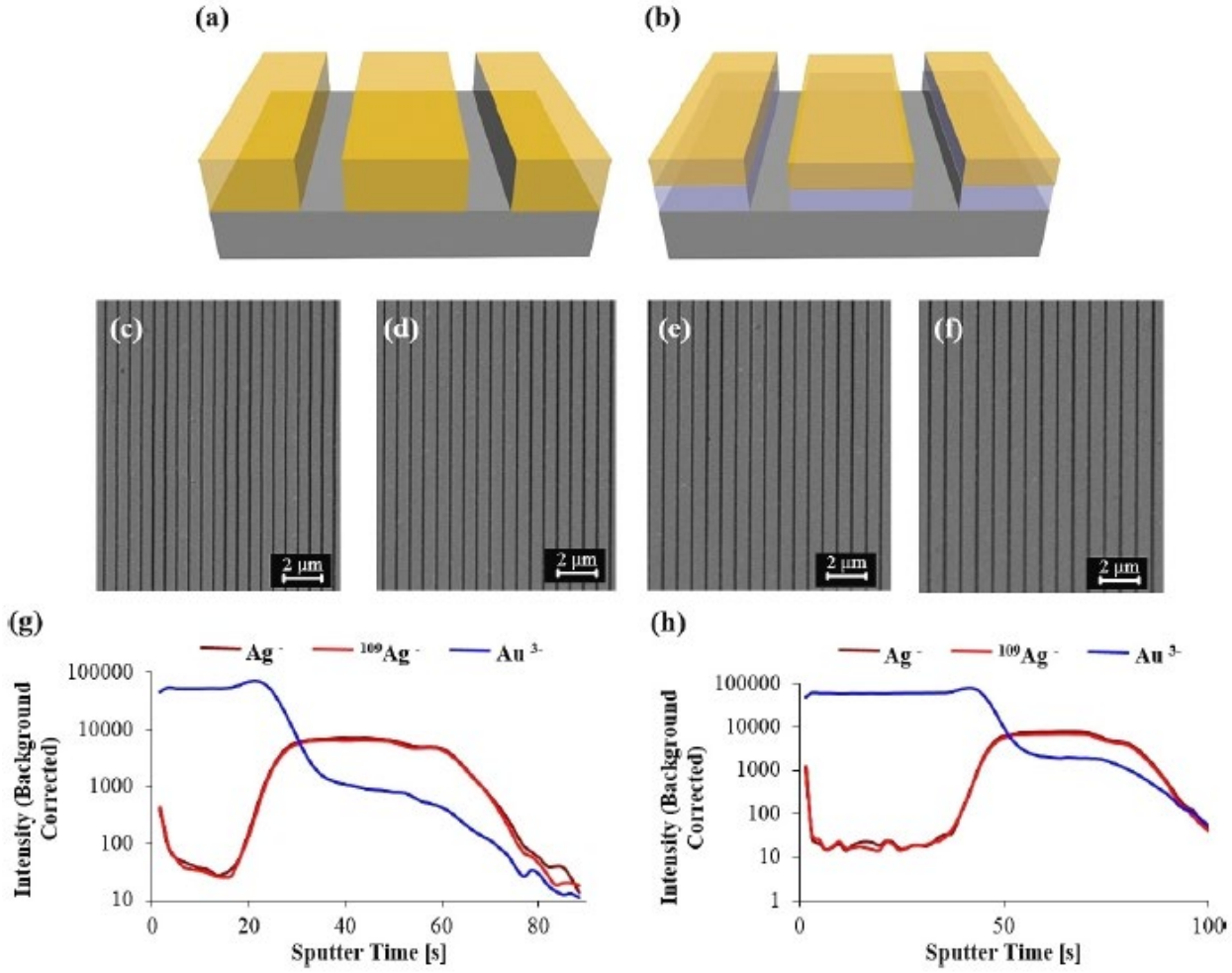

Figure 1. A schematic drawing of **(a)** gold nanoslit structure and **(b)** bimetallic nanoslit structure. SEM images of a representative Ag/Au bimetallic nanoslit array with 50 nm width and a periodicity of **(c)** 550 nm **(d)** 600 nm **(e)** 650 nm **(f)** 700 nm. Results of SIMS analysis for two Ag/Au bimetallic devices **(g)** 9 months after fabrication and **(h)** 10 months after fabrication. (SEM images of Au nanoslit devices in Fig. S1)

2 Results and Discussion

2.1 Metallic Nanoslit Film and Characterization:

Metallic nanoslit films in Au and Ag/Au bimetallic were designed and fabricated. Figure 1 shows the structure and scanning electron microscopy (SEM) images for various periodicities (550 nm, 600 nm, 650 nm, and 700 nm) at 50 nm slit widths. The metal film was 100 nm thick. The SEM images clearly show straight nanoslit arrays in metallic films.

Stability of the bimetallic layers is important for this research. It is documented that silver and gold readily diffuse into one another in liquid and solid states.[23] Secondary ion mass spectrometry (SIMS) was used to investigate grain boundary diffusion of silver into gold in these bimetallic films. SIMS samples consisted of a range of Ag:Au ratios and covered a range of ages over a period of 10 months. Figure 1 shows that little inter-diffusion was observed for any of these films. The results of the SIMS analyses support the hypothesis that there is a distinct bimetallic interface and that the bimetallic film does not change over time. A clean, distinct bimetallic interface also helped simplify the simulation studies and experiments.

2.2 Transmission SPR Spectra

The bimetallic substrates showed a strong correlation between nanoslit period and transmission peak wavelength (Figure 2a). This is consistent with the FDTD results (Figure 2b). The primary resonant peak wavelength values were plotted as a function of nanoslit period for FDTD results and experimental results (Figure 2c). There is a linear relationship between the nanoslit period and the primary resonant peak wavelength, which can be explained by the following Equation:[13]

$$\lambda_{SP} = P\sqrt{\frac{\varepsilon_m \varepsilon_d}{\varepsilon_m + \varepsilon_d}} = P\sqrt{\frac{\varepsilon_m \eta^2}{\varepsilon_m + \eta^2}} \quad (1)$$

where λ_{SP} is the resonant surface plasmon wavelength, P is the periodicity between the nanostructures, ϵ_m is the dielectric constant of the metal, ϵ_d is the dielectric constant of the liquid dielectric (the sensing area), and n is the RI.[24] The aqueous media above the metal makes up ϵ_d . Hence, increasing the periodicity will result in increased primary resonant peak wavelength.

The EOT of a thin film nanostructure is important for SPR-based sensing. To verify that age would not adversely affect the optical properties of the bimetallic nanoslit films, transmission SPR (tSPR) spectra were collected in air over a 3-week period with no notable shift in the primary resonant peak wavelength. Furthermore, the tSPR spectra were collected in wavelength shift mode, as verified in Figure 2e. Ethanol-water mixtures were passed over a chip with 50 nm slits and a 550 nm periodicity for the temperature investigation. The temperature was altered with a heat gun and monitored by two thermocouples, with one placed on the chip and a second measuring the atmospheric temperature inside of an enclosed experimental box. The primary peak at 856 nm does not have an obvious shift between 27 °C and 38 °C, indicating its good stability. In addition, the heating is primarily applied to the metallic film and not the flowing ethanol-water solution. Coupled with the SIMS results above, the bimetallic nanoslit films showed non-diffusing and long-term stable properties.

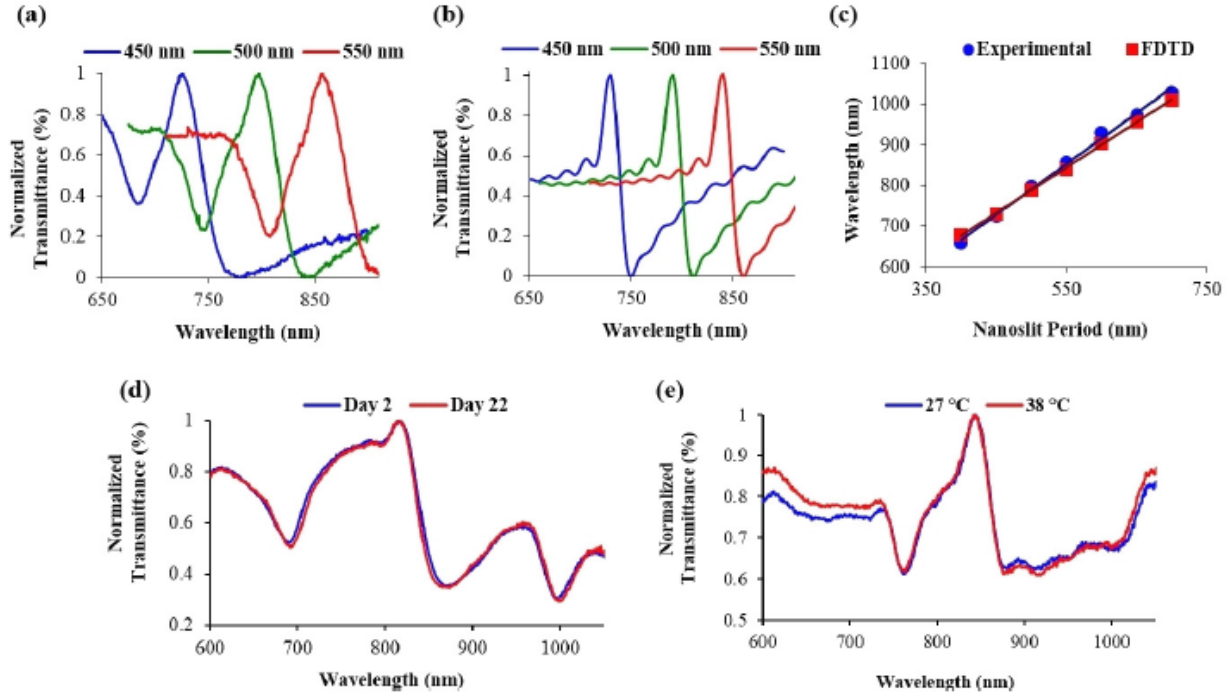

Figure 2. (a) Experimental and **(b)** FDTD simulation results showing the correlation of resonant peak position with nanoslit period for 450 nm, 500 nm, and 550 nm period arrays. **(c)** Correlation of the primary resonant peak wavelength with nanoslit period for FDTD simulation and experimental data. **(d)** Transmission spectrum of a bimetallic chip with 50 nm slits collected in air for investigation of optical stability over time. **(e)** The effect of temperature on spectral output using 50 nm slits in an ethanol-water solution.

2.3 SP Generation Analysis of Metallic Nanoslit Films

It is important to study the SP generation of the metallic nanoslit films with respect to tuning the optical transmission and its sensitivity to the dielectric environment. There are several parameters that can be adjusted to enhance the RI sensitivity in surface plasmon resonance.[25] Regarding the geometric diffraction with the bounded SPP modes launching on the flat interfaces surrounding the slits, a mechanistic description for SP generation is needed, especially the SPP scattering coefficients and efficiencies at the slit apertures. Note that SP generation efficiency is defined as the rate of SPP launching, propagation and scattering by matching the continuous electromagnetic fields quantities at the interface.[26] The schematic (Figure 3a,b) illustrates the parameters for the nanoslit structure and SP generation by a plane wave at normal incidence. The w represents the slit widths, and the $\alpha^{-}_{(top)}$, $\alpha^{+}_{(top)}$, $\alpha^{-}_{(Ag)}$, $\alpha^{+}_{(Ag)}$, $\alpha^{-}_{(Au)}$, $\alpha^{+}_{(Au)}$ represent the SP generation coefficients at the two interfaces (red and blue arrows, respectively) with inverse propagation directions. The refractive indexes inside the slits and at the outer slits are presented by n_{air} of 1, and that for the SiO_2 is presented by n_{SiO2} of 1.41.[27] Note that we focus on the SP generation at the flat metal/medium interfaces upon light excitation without considering subwavelength thickness of the metallic film. The SP generation efficiency values (e) at the Ag–SiO_2 and Au–SiO_2 interfaces are plotted as a function of wavelength λ and scaled width w' from the visible to near-infrared (600-1200 nm) obtained by the semi-analytical model,

with Ag–SiO_2 interface as $e_{(Ag)}=|\alpha^{-}_{(Ag)}(w/2)|^2=|\alpha^{+}_{(Ag)}(w/2)|^2$ (Figure 3c), Au–SiO_2 interface as $e_{(Au)}=|\alpha^{-}_{(Au)}(w/2)|^2=|\alpha^{+}_{(Au)}(w/2)|^2$ (Figure 3d), the $e_{(top)}$ as the same for both two nanoslit structures (Fig. S2). The SP generation is efficient at visible frequencies while e rapidly decreases with the increase of wavelength. Moreover, at a visible wavelength of 600 nm, the SP generation efficiencies are 0.372 at Ag–SiO_2 interface, 0.457 at Au-SiO_2 interface for 50 nm slit width and 0.346 at Ag–SiO_2 interface, 0.429 at Au-SiO_2 interface for 100 nm slit width. However, with the increase of wavelength, the SP generation efficiencies for 50 nm slit width are smaller than those for 100 nm slit width. It is expected that the total SP generation efficiency (e) will result from a "superposition" of the SPP arising from all the interfaces of the nanoslit structure. The maximum e is calculated as 0.603 (50 nm slit width) and 0.569 (100 nm slit width) for the bimetallic nanoslit structure with the incident wavelength of 600 nm. In contrast, FDTD simulation of transverse electro-magnetic field intensity for the 50–450 nm bimetallic nanoslit structure and 100–450 nm bimetallic nanoslit structure with hot spots were plotted as Figure 3e,f. Compared to gold nanoslit structure (Fig. S3), the electro-magnetic field distributions reveal that the plasmonic excitations arise from the Ag-SiO_2 interface and the Au/air interface with the strength of Ag-SiO_2>Au-air, which is consistent with the results of the semi-analytical model for SP generation efficiencies of $e_{Ag} > e_{top}$ for the bimetallic nanoslit structure.

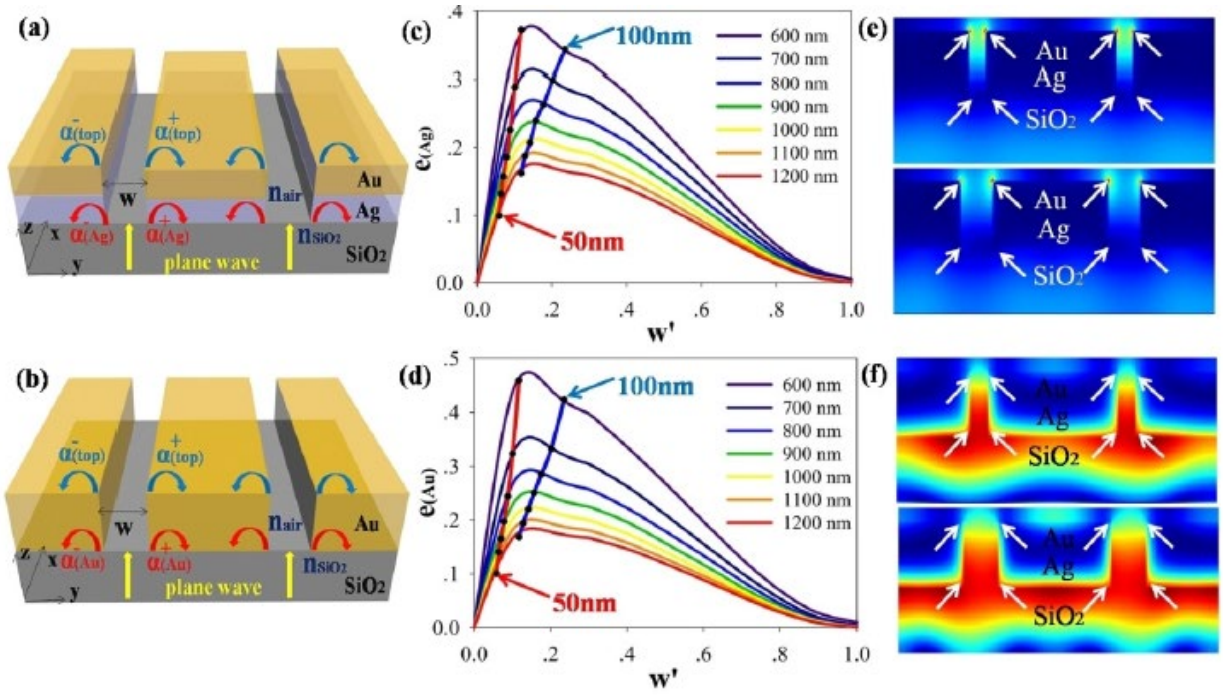

Figure 3. Semi-analytical analysis of SP generation and FDTD simulation of nanoslit array. **(a) - (b)** The schematic illustrates the parameters for the nanoslit structure and surface plasmon generation by a plane wave at normal incidence. **(a)** Bimetallic nanoslit structure. **(b)** Au nanoslit structure. **(c) - (d)** The SP generation efficiencies e at the Ag–SiO_2 and Au–SiO_2 interfaces are plotted as a function of wavelength λ and scaled width w' obtained by the semi-analytical model. **(e) - (f)** FDTD simulation of transverse electro-magnetic field intensity for the 50–450 nm bimetallic nanoslit structure and 100–450 nm bimetallic nanoslit structure with hot spots as write arrows shown. **(e)** Transverse electric field intensities of 50–450 nm nanoslit structure (top) and 100–450 nm nanoslit structure (bottom). **(f)** Transverse magnetic field intensity of 50–450 nm nanoslit structure (top) and 100–450 nm nanoslit structure (bottom).

2.4 Responses to Refractive Index Changes

To compare the bulk sensitivity between gold and bimetallic devices, a series of glycerol-water solutions (0%-20%) were made, since glycerol-water mixtures have a linear relationship between RI and increasing glycerol percentage. The results for 50 nm slit, 450 nm period devices are shown for gold (Figure 4a) and for bimetallic (Figure 4b) chips. The slope of the plots in Figure 4c and 4d show that the gold chip had a sensitivity of 473 nm/RIU while the bimetallic was 526 nm/RIU, which agrees with the reports of bimetallic layer vs. single gold layer for fiber-optic or waveguide SPR sensors.[19f,19g] And the sensitivity of the bimetallic nanoslit array reported here is much higher than that obtained by the bimetallic nanohole array (269 nm/RIU) for tSPR sensors.[21]

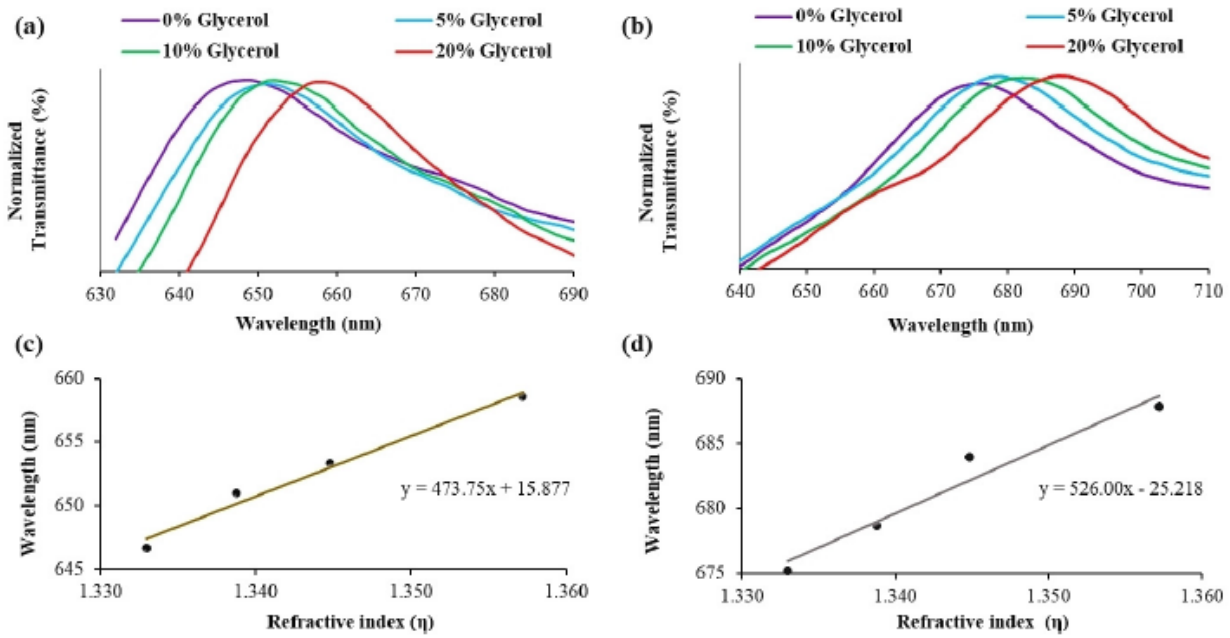

Figure 4. Transmission spectra of **(a)** Au and **(b)** Ag/Au devices in glycerol/water solutions. Sensitivity determination for **(c)** Au and **(d)** Ag/Au devices.

The surface sensitivity was further investigated by use of self-assembly. A clean nanoslit device (Figure 5a) was then exposed to 16-mercaptohexadecanoic acid (16-MHDA) which was used as a self-assembled monolayer (SAM). A schematic of a nanoslit device with bound SAM is shown in Figure 5b. The binding event was monitored by a shift in the resonant peak wavelength and the gold chip had a peak wavelength shift of 2.5 nm while the bimetallic was 6.5 nm (Figure 5c). Note that 5 mM of the thiol, in ethanol, was flushed over the chip with a syringe pump. The total SP generation efficiency change has the similar dependence on the bulk media RI changes as the EOT peak shift. Considering that the RI near the metallic surfaces is increased inside the bimetallic nanoslit structure due to the addition of SAM induced RI change, the red shift of the optical transmission after SAM formation is correlated to the decreased SP generation efficiency from 0.603 to 0.537.[28]

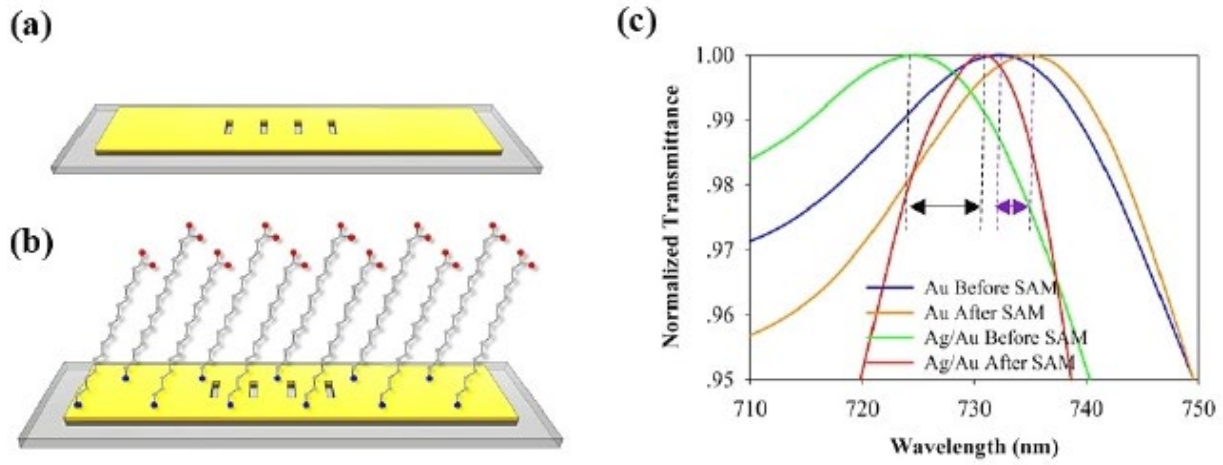

Figure 5. Schematic of the nanoslit device **(a)** before binding of the SAM and **(b)** after the SAM formation. **(c)** Detection of SAM at the Au and Ag/Au devices.

3 Conclusion

SPR on a silver/gold bimetallic substrate was shown to be stable without obvious inter-diffusion. The primary resonant peak was tunable with nanoslit periodicity. Increasing the period increased the resonant peak wavelength. The period to resonant peak wavelength behavior mirrored that of the FDTD simulations studies. The bulk sensitivity and surface sensitivity to RI changes were increased with the bimetallic devices as compared to the gold devices. Alkanethiols self-assembled and afforded a peak shift by the EOT spectra, by which the binding event was monitored. The bimetallic sensor devices were shown to be stable over time, with an improvement in sensitivity over the gold control devices. The bimetallic substrate afforded the sensitivity of silver along with the chemical stability of gold.

Acknowledgements. The authors acknowledge the financial support from US NSF grant (# 1511194) and UNCG faculty first scholarship. This work was performed at the Joint School of Nanoscience and Nanoengineering (JSNN), a member of Southeastern Nanotechnology Infrastructure Corridor (SENIC) and National Nanotechnology Coordinated Infrastructure (NNCI), which is supported by the National Science Foundation (ECCS-1542174).

Conflict of interest. The authors declare no conflict of interest.

References

1. W. L. Barnes, A. Dereux, T. W. Ebbesen, *Nature* 2003, **424**, 824– 830.

2. D. Habauzit, J. Chopineau, B. Roig, *Anal. Bioanal. Chem.* 2007, **387**, 1215– 1223.

3. Y.-T. Long, *Localized surface plasmon resonance based nanobiosensors* , Springer, Heidelberg ; New York, **2014** .

4. Y. Xia, N. J. Halas, *MRS Bull.* 2005, **30**, 338– 348.

5. A. Paul, B. Kenens, J. Hofkens, H. Uji-i, *Langmuir* 2012, **28**, 8920– 8925.

6. G. Chirico, *Gold Nanostars [electronic resource] : Synthesis, Properties and Biomedical Application* , Springer, Cham, **2015** .

7. D. Correia-Ledo, K. F. Gibson, A. Dhawan, M. Couture, T. Vo–Dinh, D. Graham, J.-F. Masson, *J. Phys. Chem. C* 2012, **116**, 6884– 6892.

8. X. Zheng, Y. Peng, X. Cui, W. Zheng, *Mater. Lett.* 2016, **173**, 88– 90.

9. X. Guo, J. Du, X. Luo, C. Du, Y. Guo, *Microelectron. Eng.* 2007, **84**, 1037– 1040.

10. S. A. Maier, *Plasmonics [electronic resource]: fundamentals and applications* , Springer, New York, **2007** .

11. K. Yu, M. S. Devadas, T. A. Major, S. S. Lo, G. V. Hartland, *J. Phys. Chem. C* 2014, **118**, 8603– 8609.

12a. Z. Zeng, X. Shi, T. Mabe, S. Christie, G. Gilmore, A. W. Smith, J. Wei, *Anal. Chem.* 2017, **89**, 5221– 5229;

12b. J. Wei, S. Singhal, D. H. Waldeck, M. J. Kofke *, Vol. US 8158409 B2*, U. S. A., 2012;

12c. J. Wei, M. Kofke, M. Rexius, S. Singhal, Y. Wang, D. H. Waldeck, *NSTI-Nanotech.* 2011, **3**, 79– 82.

13. K.-L. Lee, W.-S. Wang, P.-K. Wei, *Plasmonics* 2008, **3**, 119– 125.

14. G. V. Naik, V. M. Shalaev, A. Boltasseva, *Adv. Mater.* 2013, **25**, 3264– 3294.

15. A. Boltasseva, H. A. Atwater, *Science* 2011, **331**, 290.

16a. M. Jablan, M. Solja, H. Buljan, *Proc. IEEE* 2013, **101**, 1689– 1704;

16b. S. Xiao, X. Zhu, B.-H. Li, N. A. Mortensen, *Front. Phys.* 2016, **11**, 117801.

17. M. G. Blaber, M. D. Arnold, M. J. Ford, *J. Phys. Condens. Matter* 2010, **22**, 143201.

18. P. R. West, P. R. West, S. Ishii, G. V. Naik, N. K. Emani, *Laser Photonics Rev.* 2010, **4**, 795– 808.

19a. L. Xia, S. Yin, H. Gao, Q. Deng, C. Du, *Plasmonics* 2011, **6**, 245– 250;

19b. Y.-H. Su, W.-L. Wang, *Nanoscale Res. Lett.* 2013, **8**, 1– 6;

19c. A. K. Sharma, G. J. Mohr, *J. Phys. D* 2008, **41**, 055106;

19d. Y. K. Lee, K. S. Lee, W. M. Kim, Y. S. Sohn, *PLoS One* 2014, **9**, e 98992;

19e. Y. K. Lee, D. H. Jang, K. S. Lee, W. M. Kim, Y. S. Sohn, *Nanoscale Res. Lett.* 2013, **8**, 344;

19f. B. H. Ong, X. Yuan, S. C. Tjin, *Fiber Integrated Opt.* 2007, **26**, 229– 240;

19g. Y. Chen, Y. Yu, X. Li, Z. Tan, Y. Geng, *Plasmonics* 2015, **10**, 1801– 1808;

19h. A. Garreau, M. Tabatabaei, R. Hou, G. Q. Wallace, P. R. Norton, F. Lagugné-Labarthet, *J. Phys. Chem. C* 2016, **120**, 20267– 20276.

20a. C. Zhang, B.-Q. Chen, Z.-Y. Li, Y. Xia, Y.-G. Chen, *J. Phys. Chem. C* 2015, **119**, 16836– 16845;

20b. J. E. Lee, K. Chung, Y. H. Jang, Y. J. Jang, S. T. Kochuveedu, D. Li, D. H. Kim, *Anal. Chem.* 2012, **84**, 6494– 6500;

20c. R. Arenal, L. Henrard, L. Roiban, O. Ersen, J. Burgin, M. Treguer-Delapierre, *J. Phys. Chem. C* 2014, **118**, 25643– 25650.

21. M.-P. Murray-Méthot, M. Ratel, J.-F. Masson, *J. Phys. Chem. C* 2010, **114**, 8268– 8275.

22. D.-S. Kim, S.-H. Ahn, J. Kim, D. Seo, H. Song, Z. H. Kim, *J. Phys. Chem. C* 2016, **120**, 21082– 21090.

23a. P. A. Turner, H. C. Theuerer, K. L. Tai, *J. Vac. Sci. Technol.* 1969, **6**, 650– 650;

23b. S. K. Sen, P. M. Klugeweiss, C. L. Bauer, *J. metals* 1979, **31**, F 43-F 43;

23c. M. A. Nicolet, *Thin Solid Films* 1978, **52**, 415– 443.

24. J. Wei;, M. Kofke, S. Singhal, D. Waldeck, *JSM Nanotech. .Nanomed.* 2014, **2**.

25. A. Shalabney, A. Shalabney, I. Abdulhalim, *Laser Photonics Rev.* 2011, **5**, 571– 606.

26a. P. Lalanne, J. P. Hugonin, J. C. Rodier, *Phys. Rev. Lett.* 2005, **95**, 263902;

26b. P. Lalanne, J. P. Hugonin, J. C. Rodier, *J. Opt. Soc. Am. A* 2006, **23**, 1608– 1615.

27a. T. Murata, H. Ishizawa, I. Motoyama, A. Tanaka, *Appl. Opt.* 2006, **45**, 1465– 1468;

27b. S. Pal, G. De, *Mater. Res. Bull.* 2009, **44**, 355– 359.

28. Z. Zeng, M. N. Mendis, D. H. Waldeck, J. Wei, *RSC Adv.* 2016, **6**, 17196– 17203.